

Single-cell RNA sequencing reveals a novel cell type and immunotherapeutic targets in papillary thyroid cancer

Zhengshi Wang^{1,2,†}, Youlutuziayi Rixiati^{3,†}, Wenli Jiang^{4,†}, Chen Ye⁵, Caiguo Huang⁴, Chuangang Tang^{6,*}, Zhiqiang Yin^{1,2,*}, Binghua Jiao^{4,*}

¹ Thyroid Center, Shanghai Tenth People's Hospital, Tongji University School of Medicine, Shanghai, P.R.China;

² Shanghai Center for Thyroid Diseases, Shanghai, 200072, P.R.China;

³ Department of Pathology, Soochow University Medical School, Suzhou, 215123, P.R.China;

⁴ Department of Biochemistry and Molecular Biology, College of Basic Medical, Navy Medical University, Shanghai, 200433, P.R.China;

⁵ Department of Urology, Changhai Hospital, Navy Medical University, Shanghai, 200433, P.R.China;

⁶ Department of Thyroid and Breast Surgery, Xuzhou Central Hospital, The Affiliated Xuzhou Hospital of Medical College of Southeast University, Xuzhou, 221009, P.R.China.

[†]They contributed equally to the manuscript.

*Corresponding authors:

Binghua Jiao, PhD. Department of Biochemistry and Molecular Biology, College of Basic Medical, Navy Medical University, Shanghai, 200433, P.R.China. Tel: +86-13801924888, Email: biojiao@163.com.

Zhiqiang Yin, MD. Shanghai Center for Thyroid Diseases, No. 301, Middle Yanchang Road, Shanghai, P.R.China. Tel.: +86-18917689323, Email: 972683004@qq.com

Chuangang Tang, MD. Department of Thyroid and Breast Surgery, Xuzhou Central Hospital, The Affiliated Xuzhou Hospital of Medical College of Southeast University, Xuzhou, 221009, P.R.China. Tel.: +86-18652230137, Email: tcg3711@163.com.

30 Abstract

31 Papillary thyroid cancer (PTC) is the most common thyroid malignancy. Although
 32 PTC usually has a favorable prognosis, some aggressive PTC subtypes and lymph
 33 node (LN) metastasis contribute to high rates of recurrence and poor clinical
 34 outcomes. We analyzed single-cell RNA sequencing (scRNA-seq) data from 15
 35 samples, including primary tumors of PTC, metastatic LNs, and paracancerous tissues.
 36 After quality filtering, 28,205 cells were detected. Of these, 13,390 cells originated
 37 from 7 tumor tissues, 2,869 cells from 2 metastatic LNs, and 11,945 cells from 6
 38 paracancerous tissues. The increase in the proportion of CD4⁺ Tregs may be a key
 39 factor responsible for the immunosuppressive property of PTC. A novel cell type was
 40 identified, named Protective EGR1⁺CD4⁺ T cell, which might be antagonistic to the
 41 CD4⁺ Tregs and inhibit the formation of the immunosuppressive microenvironment
 42 and tumor immune evasion. Inhibitory checkpoints TIGIT and CD96 were found to be
 43 better targets than PD-1 for immune therapy in PTC patients with LN metastasis. For
 44 PTC patients without LN metastasis, however, PD-1, TIGIT, and CD96 could be
 45 suitable targets of immunotherapy. These findings would contribute to the further
 46 understanding of molecular mechanisms resulting in occurrence and development of
 47 PTC, and provide a theoretical rationale for targeted therapy and immunotherapy.

48 Keywords

49 papillary thyroid cancer, single-cell RNA sequencing, tumor microenvironment

50

51

52 Introduction

53 According to the GLOBOCAN database, there were an estimated 586,202 new cases
 54 of thyroid cancer worldwide in 2020 ¹. The global incidence was up to 13.1 per
 55 100,000 people, ranking 11th in occurrence rate. The most common pathological type
 56 of thyroid cancer is papillary thyroid cancer (PTC), accounting for approximately 85%
 57 of all cases ². Although PTC usually has a favorable prognosis, some aggressive PTC
 58 subtypes (e.g. tall cell variant and Hürthle cell cancer) and lymph node (LN)
 59 metastasis contribute to high rates of recurrence and poor clinical outcomes ^{3,4}. For
 60 PTC patients with a high risk of recurrence, radioiodine treatment could be used to
 61 improve their prognosis ⁵. However, some PTC patients would develop into
 62 radioiodine-refractory PTC, which in turn lead to low survival rate ^{6,7}. Therefore, a
 63 deeper understanding of molecular and cellular mechanisms of PTC would help in the
 64 development of therapeutic strategies.

65 Currently, efforts to study the tumor progression and metastatic process of
 66 thyroid cancer have mainly focused on the analysis of cancer cells using genetic
 67 aberrations^{8,9,10,11}. However, the tumor progression and metastasis are a complicated
 68 biological process, which were not only affected by the characteristic features of
 69 cancer cells themselves but also by the tumor microenvironment (TME) ^{12,13,14,15}.
 70 TME refers to a tumor pathology-related environment, comprising stromal cells,
 71 extracellular matrix (ECM), and cytokines. A comprehensive analysis of TME in PTC
 72 can reveal the key elements involved in the susceptibility of tumor-induced
 73 immunological changes, which could be employed to develop new immunotherapy
 74 strategies.

75 Genomic and transcriptomic studies have revealed a huge number of driver
 76 mutations, abnormal regulatory programs, and disease subtypes in major human
 77 tumors^{16,17,18,19}. However, the conventional bulk sequencing frequently adopted in
 78 these studies only revealed the overall biological characteristics of each tumor and
 79 lacked the ability to capture signatures in intratumoral and intercellular
 80 heterogeneity. As opposed to bulk sequencing, the emergence of single-cell RNA
 81 sequencing (scRNA-seq) provided a new opportunity to enables characterization of
 82 cell populations at the single-cell level, and made it more independent of any previous
 83 assumptions about surface markers ²⁰. scRNA-seq has been applied to investigate
 84 cellular properties in various solid tumor types ²¹. However, the single-cell atlas of

PTC remains to be fully revealed. Therefore, we analyzed primary PTC tumors, paracancerous tissues, and metastatic LNs using the scRNA-seq-based profiling method to better understand the intratumoral heterogeneity and complexity during the development of PTC.

Results

Single cell atlas and heterogeneity of PTC

A total of 15 samples from seven PTC patients were involved in this study. After quality filtering, 28,205 cells were detected. Of these, 13,390 cells originated from 7 tumor tissues, 2,869 cells from 2 metastatic LNs, and 11,945 cells from 6 paracancerous tissues (Fig. 1a and 1b). Subsequently, we partitioned the cells into 26 clusters, which were further classified into 10 major cell types based on known markers described in previous studies: B cells (CD19⁺, MS4A1⁺, CD38⁺, CD79A⁺, CD79B⁺); CD4⁺ T cells (CD3D⁺, CD4⁺); CD8⁺ T cells (CD3D⁺, CD8A⁺); endothelial cells (CD31⁺, CD34⁺); epithelial cells (EPCAM⁺, KRT18⁺); fibroblasts (COL1A1⁺); myeloid cells (CD14⁺, CD86⁺, ITGAX⁺, CD80⁺, CD83⁺, ITGAM⁺); naive T cells (CD3D⁺, CCR7⁺); natural killer T (NKT) cells (CD3D⁺, NKG7⁺); and plasma cells (CD79A⁺, SDC1⁺) (Fig. 1c, Supplementary Fig. 1 and 2).

Based on the frequencies of cell types, we detected cellular landscapes in primary tumors, paracancerous tissues, and metastatic LNs, respectively. Significant differences were observed in several cell types (Fig. 1d). The immune cells accounted for the major differences between primary tumors and paracancerous tissues, with the frequency of NKT cells and plasma cells increasing, and CD4⁺ T cells and B cells decreasing in the primary tumors ($P < 0.05$). The most striking changes between metastatic LNs and primary tumors were observed in CD8⁺ T cells. At the cluster level, there were also significant differences within the same cell types. As exemplified by myeloid cells, we observed an increase in the frequency of cluster 21 and a decrease in the proportion of cluster 25 in metastatic LNs compared with primary tumors and paracancerous tissues. These results demonstrated that the disease progression might also be somehow associated with evolutionary immune cells, reflecting the existence of heterogeneity among samples and cell populations.

To conduct the interaction network of tumor microenvironment in PTC, CellphoneDB was used to calculate potential ligand-receptor pairs in cells. And Cytoscape was performed to visualize the cell interaction. We found that myeloid cells and T cell-related cells possessed more interaction pairs with other cells than

119 others (Fig. 1e), showing the dominant roles of myeloid cells and T cells.

120 **Identification of malignant cells in epithelial cells**

121 To distinguish malignant from non-malignant cells within the epithelial cells,
122 CopyKAT was performed to identify PTC genome alterations. Despite the
123 heterogeneity, almost all malignant cells possessed deletions from chromosomes 16
124 and 19 and amplifications in chromosomes 13 (Fig. 2a and 2b). We distinguished
125 1,679 non-malignant cells and 450 cells were identified as malignant cells. Very few
126 malignant cells were also found in paracancerous tissues (Fig. 2b). In order to support
127 the identification results of the malignant cells, pseudotime trajectory analysis was
128 performed. The results showed that malignant cells were present at the end of the
129 differentiation trajectory (Fig. 2c).

130 To screen for key regulons in malignant cells, we conducted SCENIC analysis
131 and identified motifs ATF3 and BHLHE40 that were highly activated in malignant
132 cells (Fig. 2d). In a previous study, ATF3 was found to enhance breast cancer
133 metastasis³⁶. At the same time, decreased activity was found in CREM and ETS1. In
134 TCGA THCA cohort, a high level of CREM and ETS1 was significantly related to a
135 good prognosis, and BHLHE40 is highly expressed in patients with LN metastasis
136 compared with patients without LN metastasis (Fig. 2e and 2f). These results provide
137 potential targets for suppressing cells to possess malignant characteristics.

138 We further characterized the functions of differential genes between metastatic
139 LNs and primary tumors by comparing pathway activities. Pathways involved in
140 cellular component assembly, protein-containing complex assembly, and regulation of
141 microtubule motor activity were relatively upregulated in LN-derived malignant cells
142 (Fig. 2g). The results showed that malignant cells in metastatic LNs have stronger cell
143 proliferative and invasive abilities.

144 **Identification of a novel T cell type**

145 Reclustering of T cells identified 10 subclusters: CD4⁺ Tregs, Cytotoxic CD8⁺ T
146 cells, Exhausted CD4⁺ T cells, Follicular helper (Tfh) T cells, Naïve CD4⁺ T cells,
147 Naïve T cells; NKT cells, Pre-exhausted CD8⁺ T cells, Proliferating CD8⁺ T cells, and
148 Protective EGR1⁺CD4⁺ T cells (Fig. 3a and 3b). In addition to the markers used above,
149 we also found some other makers that can be used for cell population identification.
150 For example, TYMS can be used for Pre-exhausted CD8⁺ T cells identification, and
151 RTKN2 can be used for Pre-exhausted CD4⁺ Tregs identification (Fig. 3c,
152 Supplementary Fig. 3). Notably, a novel cell type was identified, which was totally

different from preconceived cellular definitions. The novel cell type specifically highly expressed EGR1, and we named it as Protective EGR1⁺CD4⁺T cells. The mRNA expression level and protein level of EGR1 were significantly decreased in tumor tissues compared with normal tissues (Fig. 3d). Survival analysis showed that patients with high EGR1 levels had a better prognosis than those with low EGR1 levels (Fig. 3e). Through cell frequency analysis, we found an interesting phenomenon that the proportion of CD4⁺ Tregs tended to increase with PTC disease progression and Protective EGR1⁺CD4⁺ T cells exhibited a quite opposite trend (Fig. 3f). The results were validated with TCGA data calculated using Cibersortx (Fig. 3g) and further validated by the changes of marker gene expression levels in the TCGA THCA cohort (Supplementary Fig. 4a). These findings indicated that both of CD4⁺ Tregs and Protective EGR1⁺CD4⁺ T cells may have an important impact on disease progression, and our newly identified cell type (Protective EGR1⁺CD4⁺T cells) may be antagonistic to the CD4⁺ Tregs.

We further characterized the functions of CD4⁺ Tregs and Protective EGR1⁺CD4⁺ T cells by comparing pathway activities. In the primary tumors, CD4⁺ Tregs and Protective EGR1⁺CD4⁺ T cells exhibited vastly different signaling pathways. CD4⁺ Tregs were related to epithelial-mesenchymal transition (EMT) and hypoxia, whereas G2M checkpoint and KRAS signaling pathway were significantly down-regulated in Protective EGR1⁺CD4⁺ T cells (Fig. 4a). In the metastatic LNs, mitotic spindle and oxidative phosphorylation were also down-regulated in Protective EGR1⁺CD4⁺ T cells (Supplementary Fig. 4b). To screen for key genes related to tumorigenesis and tumor development in CD4⁺ Tregs and Protective EGR1⁺CD4⁺ T cells, we conducted SCENIC analysis and identified essential motifs in CD4⁺ Tregs and Protective EGR1⁺CD4⁺ T cells. FOSL2, ATF3, REL, and HES1 were CD4⁺ Tregs-specific motifs. BCLAF1 and ETS1 motifs were highly activated in Protective EGR1⁺CD4⁺ T cells (Fig. 4b). These results provided potential targets for inhibiting or reversing the formation of the immunosuppressive microenvironment.

The DEGs derived from Protective EGR1⁺CD4⁺ T cells were identified, including 31 up-regulated mRNAs and 50 down-regulated mRNAs in primary tumors compared with paracancerous tissues (Supplementary Fig. 4c). The DEGs derived from CD4⁺ Tregs were also identified (Supplementary Fig. 4d). Subsequently, we examined the immune checkpoints in the cell clusters (Fig. 4c and 4d). Notably, we found that TIGIT, an inhibitory checkpoint, was upregulated in Exhausted CD4⁺ T

187 cells and CD96 was upregulated in Pre-exhausted CD8⁺ T cells in metastatic LNs. In
188 tumor tissues, PDCD1 (PD-1) and TIGIT were significantly upregulated in
189 Exhausted CD4⁺ T cells, and CD96 was significantly upregulated in Pre-exhausted
190 CD8⁺ T cells. Since TIGIT, CD96, and PDCD1 (PD-1) are markers of T cell
191 exhaustion, these data indicated that Exhausted CD4⁺ T cells and Pre-exhausted CD8⁺
192 T cells were exhausted in the tumor microenvironment, which was consistent with our
193 previous cell population classification results.

194 **Neutrophils cells are extremely reduced in tumor**

195 For exploring the heterogeneity among myeloid cells, 1607 myeloid cells were
196 clustered into 5 cell subtypes based on known markers described in previous studies:
197 macrophages, dendritic cells, monocytes, neutrophils, and myeloid-derived suppressor
198 cells (Fig. 5a and 5b). Through cell frequency analysis, a marked decrease of
199 neutrophils was observed in tumors while the proportion of macrophages increased
200 continuously as the disease progressed (Fig. 5c). The trend was consistent with TCGA
201 data calculated by ciphersortx (Fig. 5d). Survival analysis showed that disease-free
202 survival (DFS) of patients with low-level dendritic cell was longer than that of the
203 high-level group in the TCGA cohort (Fig. 5e). Similar results were observed in
204 macrophages (Supplementary Fig. 5a). However, low-level neutrophil was observed
205 to be associated with better prognosis (Supplementary Fig. 5b). These results
206 suggested that macrophages, dendritic cells, and neutrophils are more relevant to the
207 development of PTC.

208 We further characterized the functions of myeloid cell subtypes by comparing
209 pathway activities. Compared with paracancerous tissues, the cancer hallmark-related
210 pathways were relatively enriched in myeloid-derived suppressor cells from tumors,
211 whereas they were generally down-regulated in neutrophils from tumors (Fig. 6a).
212 These were consistent with the changes in cell proportions we observed earlier (Fig.
213 5c). Compared with tumor tissues, however, some cancer hallmark-related pathways
214 (i.e. mTORC1 signaling and E2F targets) were down-regulated in myeloid-derived
215 suppressor cells from metastatic LNs (Fig. 6b). The results indicated that
216 myeloid-derived suppressor cells were involved in cancer cell proliferation, but not in
217 tumor metastasis.

218 In order to screen for key genes related to tumor occurrence and development in
219 myeloid cells, we conducted SCENIC analysis and identified essential motifs in
220 myeloid cells subtypes. Similar to the results of pathway analysis, the overall

regulatory factors in neutrophils were also inconsistent with the other cell types (Fig. 6c). We recognized that the decreased activity of a lot of motifs (i.e. YY1 and IRF5) and activation of the STAT3, ZNF143, and HCFC1 motifs led to the reduction of neutrophils.

As shown in Fig. 6d, cells from myeloid cell-derived cluster 8 uniquely expressed the M1 macrophages marker CCL5, whereas M2 macrophages markers including CTSD/CTSD/FN1 were relatively highly expressed in cluster 0. The proportion of cluster 0 was high in tumors and LNs, although the difference has not reached a significant level (Fig. 5c). All of this evidence certified that cluster 0 represented an M2-like tumor-associated macrophages (TAM) cluster, the increase of which may be related to disease progression. Cluster 9 highly expressed the cytokines CCL17/CCL19/CCL22. These cytokines could bind to CCR4, a marker on the cell membrane of CD4⁺ Tregs, and showed strong chemotaxis to CD4⁺ Tregs^{37, 38}. It corroborated with our above results that the increasing trend of CD4⁺ Tregs with disease progression was coincident with that of myeloid cell-derived cluster 9 (Fig. 3f and 5c). The findings indicated that the dendritic cells (cluster 9) could recruit CD4⁺ Tregs into the tumor regions, thereby acting as an immunosuppressive effect.

Discussion

At present, the study of molecular mechanisms underlying the occurrence and development of PTC mainly focused on the genetical alteration based on bulk sequencing data. We profiled integrated and heterologous transcriptional landscapes of PTC using single-cell sequencing methods, including cancer cells and TME of primary tumors and metastatic lesions. Through sequencing 28,205 cells, we found that the majority of cell clusters possessed strong heterogeneities. Tumor heterogeneity exists in various malignancies and remains not only between tumors but also within a single tumor³⁹, which is considered as a cause of chemoresistance of cancer. In-depth knowledge of tumor heterogeneity of PTC will make molecular testing more reliable and accurate prior to surgery (whether to undergo the surgery or close follow-up only), and benefit to stratify the recurrence risk and personalized precision treatment (thyroidectomy or total thyroidectomy or plus radioiodine treatment). On the other hand, TME on disease progression and metastasis has also been confirmed in numerous diseases^{40, 41}. Investigations of TME-related cellular and molecular events will provide a theoretical rationale for drug discovery and development, especially for targeted therapy and immunotherapy.

In addition to previously described cell types, we discovered a novel cell subpopulation, named Protective EGR1⁺CD4⁺T cells. EGR1 is a transcription factor primarily mediate cellular functions (i.e. cell growth, cancer progress and apoptosis) via the RAS/RAF/MEK/ERK signaling pathway⁴², which was a hallmark of PTC⁴³. It has also been previously reported that p53 could bind to EGR1 promoter and subsequently resulted in efficient apoptosis⁴⁴. EGR1 was usually considered a tumor suppressor in many human malignancies including PTC^{45, 46, 47, 48}. By comparing the proportion of cells from different tissues and pathway enrichment analyzing, we found that KRAS signaling pathway (part of RAS/RAF/MEK/ERK signaling pathway) was significantly down-regulated in Protective EGR1⁺CD4⁺ T cells. It indicated that Protective EGR1⁺CD4⁺T cells might inhibit the formation of the immunosuppressive microenvironment and tumor immune evasion via RAS/RAF/MEK/ERK signaling pathway, thereby restraining tumor growth. Therefore, EGR1 might represent a potential therapeutic target for PTC.

CD4⁺ Tregs, were overall considered to disrupt anti-tumor immunity and then help tumor cells to achieve immune evasion, leading to the tumor growth and metastasis⁴⁹. Our results also showed that CD4⁺ Tregs had the greatest positive correlation with the process of EMT, which matched those reported in other studies of PTC patients⁵⁰. Using pathway enrichment analysis, we found that relevant pathways associated with CD4⁺ Tregs and Protective EGR1⁺CD4⁺T cells were almost the opposite. The proportion of CD4⁺ Tregs among three samples increased in the disease progression order (paracancerous tissues < tumors < LNs) while the proportion of Protective EGR1⁺CD4⁺T cells decreased sequentially. This strongly suggested that CD4⁺ Tregs and Protective EGR1⁺CD4⁺T cells might act antagonistically to each other.

Immunotherapy is an emerging method for cancer treatment and promising results have been obtained in both hematologic and solid tumors^{51, 52}. T cell exhaustion is a critical mechanism of immune evasion. Blockade the PD1/PDL1 interaction to reverse T cell exhaustion is considered a milestone achievement in the field of immunotherapy^{53, 54, 55}. Our results showed that PDCD1 (PD-1), TIGIT, and CD96 could be suitable targets of immunotherapy in PTC patients without LN metastasis since they were upregulated in tumor tissues. However, the expression levels of TIGIT and CD96 were much higher than that of PDCD1 (PD-1) in LN-derived exhausted T cell types (Exhausted CD4⁺ T cells and Pre-exhausted CD8⁺

289 T cells). Therefore, TIGIT and CD96 might be better therapeutic targets for
 290 immunotherapy in PTC patients with LN metastasis than PDCD1 (PD-1). Jill et al.⁵⁶
 291 investigated the CD4⁺ and CD8⁺ T cell exhaustion in PTC patients with LN metastasis
 292 using flow cytometry, and found that CD8⁺ T cell exhaustion was incomplete. This
 293 was most likely because TIGIT and CD96 were not included into analysis in their
 294 study, both of which were very important inhibitory immune checkpoints. However,
 295 their findings supported our conclusions to some extent that PDCD1 (PD-1) was not a
 296 suitable molecular target for the treatment of PTC with LN metastasis.

297 We initially applied a commonly used method inferCNV for the identification of
 298 malignant cells⁵⁷, which was shown to be unable to identify efficiently malignant
 299 tumor cells from epithelial cells in this study. Thus, we adapted an integrative
 300 Bayesian segmentation approach called CopyKAT and solved the conundrum
 301 successfully³⁵. As a result, more than half of tumor-derived epithelial cells were
 302 non-malignant cells, which might well explain the reason for the indolent clinical
 303 behavior of PTC. Additionally, there were also a very small number of malignant
 304 epithelial cells in paracancerous tissues, possibly due to the presence of the pre-tumor
 305 microenvironment in paracancerous tissues. There were several possible reasons. First,
 306 the pre-metastatic niche, a favorable microenvironment to tumor metastasis, formed in
 307 paracancerous tissues⁵⁸, and in turn lead to intra-thyroid metastasis. The concept of
 308 intra-thyroid metastasis of thyroid cancer has not been described yet. The reason is
 309 possibly caused by the small size of the thyroid gland itself and the narrow lumen of
 310 artery/vein nourishing the thyroid gland. As is well-known, liver cancer tends to
 311 present with intrahepatic metastatic disease, mainly due to the large diameter of the
 312 portal vein and hepatic artery. Second, multifocal PTC has already existed within the
 313 thyroid gland, whereas the extremely tiny lesion cannot be detected under
 314 microscopic examination. Based on the two points above, thyroidectomy is
 315 necessary to be performed for patients with PTC at least to ensure a total removal of
 316 potential lesions. Third, CopyKAT is not able to discriminate malignant cells from
 317 non-malignant cells with hundred percent accuracy.

318 In summary, we initially investigated the single-cell level heterogeneity of
 319 primary PTC tumors and metastatic lesions. A novel cell type, named Protective
 320 EGR1+CD4⁺T cells, was identified, which might inhibit the formation of the
 321 immunosuppressive microenvironment and tumor immune evasion. TIGIT and CD96
 322 might be better therapeutic targets for immunotherapy in PTC patients with LN

323 metastasis than PDCD1 (PD-1). These findings would contribute to the further
324 understanding of molecular mechanisms resulting in occurrence and development of
325 PTC, and provide a theoretical rationale for targeted therapy and immunotherapy.

326

327 **Methods**

328 **Sample collection and clinical information**

329 Seven patients diagnosed with PTC were obtained from Shanghai Tenth People's
330 Hospital. A total of 15 tissue samples (7 tumor tissues, 6 paracancerous tissues, and 2
331 metastatic LNs) were obtained from 7 PTC patients. Written informed consent was
332 obtained from all patients in the present study. Histological diagnosis of all the
333 samples was confirmed by the pathology department.

334 **Tissue digestion and single-cell suspension preparation**

335 Cells of each sample were firstly stained with two fluorescent dye, Calcein AM
336 (Thermo Fisher Scientific Cat. No. C1430) and Draq7 (Cat. No. 564904), for
337 precisely determination of cell concentration and viability via BD Rhapsody™
338 Scanner before single-cell multiplexing labeling. The cells of each sample were
339 sequentially labeled with BD Human Single-Cell Multiplexing Kit (Cat. No. 633781)
340 which utilizing an innovative antibody-oligo technology²² mainly to provide higher
341 sample throughput and eliminate batch effect for single-cell library preparation and
342 sequencing. A set of 12 antibodies in this kit recognize the same universally expressed
343 cell-surface antigen of human cells. Each antibody is conjugated with a Sample Tag, a
344 unique 45-nucleotide barcode sequence. Briefly, cells from each sample were labeled
345 by antibodies with different sample tags respectively and washed twice with BD
346 Pharmingen™ Stain Buffer (FBS) (Cat. No. 554656) before pooling all samples
347 together. BD Rhapsody Express system²³ based on Fan et al. was utilized for
348 single-cell transcriptome capture. Pooled samples were then loaded in one BD
349 Rhapsody™ Cartridge that was primed and treated strictly following the
350 manufacturer's protocol (BD Biosciences). Cell Capture Beads (BD Biosciences)
351 were then loaded excessively onto the cartridge to ensure that nearly every micro-well
352 contains one bead, and excess beads were washed away from the cartridge. Viable
353 cells with beads captured in wells were detected in BD Rhapsody™. Then cells were
354 lysed, Cell Capture Beads were retrieved and washed before performing reverse
355 transcription and treatment with exonuclease I.

356 **Library construction and sequencing**

357 Transcriptome and SampleTag information of single-cells was obtained through BD
358 Rhapsody System. Microbeads-captured single cell transcriptome and SampleTag
359 sequences were generated into the cDNA library and SampleTag library separately

360 containing cell labels and unique molecular identifiers (UMI) information. Briefly,
361 double-strand cDNA was firstly generated from microbeads-captured single-cell
362 transcriptome through several steps including reverse transcription, second-strand
363 synthesis, end preparation, adapter ligation, and whole transcriptome amplification.
364 Then final cDNA library was generated from double-strand full-length cDNA by
365 random priming amplification with BD Rhapsody cDNA Kit (BD Biosciences,
366 Catalog No.: 633773) and BD Rhapsody Targeted mRNA & AbSeq Amplification Kit
367 (BD Biosciences, Catalog No.: 633774). On the other hand, the SampleTag library
368 was generated from microbeads-captured single-cell SampleTag sequences through
369 several steps including reverse transcription, nest PCR, and final index PCR. Libraries
370 were sequenced on the NovaSeq platform (Illumina).

371 **Raw data preprocessing and quality control**

372 Raw sequencing reads of the cDNA library and SampleTag library were processed
373 through the BD Rhapsody Whole Transcriptome Assay Analysis Pipeline (Early
374 access), which included filtering by reads quality, annotating reads, annotating
375 molecules, determining putative cells, and generating single-cell expression matrix.
376 Briefly, read pairs with low sequencing quality were firstly removed. The
377 quality-filtered R1 reads were analyzed to identify the sequence of cell labels, UMI
378 sequence, and poly-dT tail sequence, meanwhile the quality-filtered R2 reads were
379 mapped to Genome Reference Consortium Human Build 38 (GRCh38) using STAR
380 (version 2.5.2b) in the reads annotation step. Further adjustment was performed with
381 the recursive substitution error correction (RSEC) and distribution-based error
382 correction (DBEC) algorithms to remove artifact molecules due to amplification bias
383 in the molecules annotation step. Putative cells were distinguished from background
384 noise with second derivative analysis in the putative cell determination step. Finally,
385 putative cells information was combined with molecules adjusted by the recursive
386 substitution error correction and distribution-based error correction algorithms to
387 generate a single-cell expression matrix. The pipeline also determined the sample
388 origin of every single cells via the sample determination algorithm according to the
389 sequencing reads of the SampleTag library. The algorithm classified all putative single
390 cell into three categories: Multiplet, two or more SampleTag exceed their minimum
391 thresholds, indicating more than one actual cell in one micro-well. Undetermined, not
392 enough SampleTag reads for the sample origin. SampleTag01-12, only one
393 SampleTag exceed their minimum thresholds. . Among all the output files, Matrix for

UMI counts per cell corrected by DBEC and SampleTag annotation result were used for downstream clustering analysis.

Dimension reduction and clustering

The R package Seurat²³ was utilized for subsequent analysis. Raw gene expression matrices from the cartridge were read into R (version 3.6.0) and converted to Seurat objects. Cells label as “Undetermined” and “Multiple” were excluded in the following analysis. The gene expression matrix was then normalized to the total cellular UMI count. Top 2000 features were selected as highly variable genes for further clustering analysis. In order to reduce dimensionality, PCA was performed based on the highly variable genes after scaling the data with respect to UMI counts. On top of that, the first 9 principal components were chosen for downstream clustering based on the heatmap of principle components, and the elbow plot of principle components to further reduce dimensionality using the UMAP algorithm. The transcriptional markers of each cluster were calculated using the FindAllMarkers function with the MAST package to run the DE testing under the following criteria: log2 fold change > 0.1; p < 0.05; min. percentage > 0.25. Top 500 markers of each cluster were then selected to perform a heatmap plot.

Cell annotation and cell type identification

Cell populations were matched to cell types based on the expression of known marker genes and previously identified expression signatures^{23, 24, 25, 26, 27, 28}.

Comparison of cell clusters and cell type proportion

The change in the fraction of the different cell types was separately computed for each sample across all clusters, as the fraction of cell in each cluster, out of the total number of cells²⁹. To assess a statistically significant difference in a fraction of a specific cell type, we performed paired t-test.

Significantly dysregulated genes identification

We identified differentially expressed genes (DEGs) based on analysis of the MAST package using the R. The threshold of DEGs was set as: 1) P-value of F test < 0.05; 2) |FC| ≥ 1.5.

External data validation with TCGA datasets

CIBERSORTx was used to detect the abundance of cell types identified in the present work in bulk RNA-seq data³⁰. After calculated the relative abundance of each cell type, we divided the patients into two groups: high 50% and low 50%. Subsequently, Kaplan-Meier analysis was performed using ggsurvplot function of the R package

428 ‘survminer’. Whether the occurrence of cell types in the different subgroups showed
429 significant differences was evaluated by Wilcoxon test.

430 **Functional annotation and enrichment**

431 GO enrichment and KEGG enrichment of DEGs were performed using Fisher exact
432 test with Benjamini-Hochberg multiple testing adjustment. The results were
433 visualized using R package. Gene set variation analysis (GSVA)³¹ was performed
434 using 50 hallmark-related gene sets, as described in the GSVA package.

435 **Identification of hub regulons with SENIC**

436 In order to investigate the gene regulatory network of different sample groups, we
437 utilized SCENIC³² using the R.

438 **Cell-cell communication analysis based on ligand-receptor pairs**

439 Cell-cell communication at the molecular level was analyzed with CellPhoneDB³³.

440 **Cell trajectory analysis with Monocle**

441 In order to reveal the development of malignant cells, we employed Monocle 2, an R
442 package designed for single cell trajectories³⁴. After obtaining the differentially
443 expressed genes through differential Gene Test function, the trajectories were
444 visualized as 2D tSNE plots.

445 **Drug-target analysis with TCMID database**

446 After obtaining the differentially expressed genes, we obtain the targeted relationship
447 between drugs and genes from the TCMID database
448 (<http://www.megabionet.org/tcmid>).

449 **CNV Estimation**

450 CopyKAT³⁵ (Copynumber Karyotyping of Tumors), a R package was performed to
451 separate tumor cells from normal cells using high-throughput sc-RNAseq data. Cells
452 with extensive genome-wide copy number aberrations (aneuploidy) are considered as
453 tumor cells, whereas stromal normal cells and immune cells often have 2N diploid or
454 near-diploid copy number profiles.

455 **Statistical analysis**

456 Box plots were drawn with the R base package. Hence, the boxes span from the 25th
457 to the 75th percentiles. Violin plots were generated by the ggplot2 R package.
458 Unpaired two-tailed t-tests was used to compare the difference between two groups.
459 While One-way analysis of variance (ANOVA) was used for multiple group
460 comparisons.

461 **Data availability**

462 The cancer genome atlas (TCGA) thyroid cancer (THCA) cohort were downloaded
463 from UCSC XENA (<http://xena.ucsc.edu/>).

464

465 **References**

466 1. Sung H, *et al.* Global cancer statistics 2020: GLOBOCAN estimates of incidence and
467 mortality worldwide for 36 cancers in 185 countries. (2021).

468

469 2. Fagin JA, Wells SA, Jr. Biologic and Clinical Perspectives on Thyroid Cancer. *N Engl J*
470 *Med* **375**, 1054-1067 (2016).

471

472 3. Yu J, *et al.* Lymph node metastasis prediction of papillary thyroid carcinoma based on
473 transfer learning radiomics. *Nat Commun* **11**, 4807 (2020).

474

475 4. Cohen EE, *et al.* Axitinib is an active treatment for all histologic subtypes of advanced
476 thyroid cancer: results from a phase II study. *J Clin Oncol* **26**, 4708-4713 (2008).

477

478 5. Jiao C, *et al.* REGgamma ablation impedes dedifferentiation of anaplastic thyroid
479 carcinoma and accentuates radio-therapeutic response by regulating the
480 Smad7-TGF-beta pathway. *Cell Death Differ* **27**, 497-508 (2020).

481

482 6. Laetitia G, Sven S, Fabrice J. Combinatorial Therapies in Thyroid Cancer: An
483 Overview of Preclinical and Clinical Progresses. *Cells* **9**, (2020).

484

485 7. Hong CM, Ahn BC. Redifferentiation of Radioiodine Refractory Differentiated Thyroid

486 Cancer for Reapplication of I-131 Therapy. *Front Endocrinol (Lausanne)* **8**, 260
487 (2017).
488
489 8. Shen X, *et al.* Patient Age-Associated Mortality Risk Is Differentiated by BRAF V600E
490 Status in Papillary Thyroid Cancer. **36**, 438-445 (2018).
491
492 9. Pozdeyev N, *et al.* Genetic Analysis of 779 Advanced Differentiated and Anaplastic
493 Thyroid Cancers. **24**, 3059-3068 (2018).
494
495 10. Liu R, Bishop J, Zhu G, Zhang T, Ladenson P, Xing MJJo. Mortality Risk Stratification
496 by Combining BRAF V600E and TERT Promoter Mutations in Papillary Thyroid
497 Cancer: Genetic Duet of BRAF and TERT Promoter Mutations in Thyroid Cancer
498 Mortality. **3**, 202-208 (2017).
499
500 11. Li Y, *et al.* CYP2S1 is a synthetic lethal target in BRAF-driven thyroid cancers. **5**, 191
501 (2020).
502
503 12. Tekpli X, *et al.* An independent poor-prognosis subtype of breast cancer defined by a
504 distinct tumor immune microenvironment. *Nat Commun* **10**, 5499 (2019).
505
506 13. Roehlecke C, Schmidt MHH. Tunneling Nanotubes and Tumor Microtubes in Cancer.
507 *Cancers (Basel)* **12**, (2020).

508

509 14. Oczko-Wojciechowska M, *et al.* Impact of the Tumor Microenvironment on the Gene

510 Expression Profile in Papillary Thyroid Cancer. *Pathobiology* **87**, 143-154 (2020).

511

512 15. Jolly LA, *et al.* Fibroblast-Mediated Collagen Remodeling Within the Tumor

513 Microenvironment Facilitates Progression of Thyroid Cancers Driven by BrafV600E

514 and Pten Loss. *Cancer Res* **76**, 1804-1813 (2016).

515

516 16. Robertson A, *et al.* Identification of Differential Tumor Subtypes of T1 Bladder Cancer.

517 **78**, 533-537 (2020).

518

519 17. Mer A, *et al.* Biological and therapeutic implications of a unique subtype of NPM1

520 mutated AML. **12**, 1054 (2021).

521

522 18. Job S, *et al.* Identification of Four Immune Subtypes Characterized by Distinct

523 Composition and Functions of Tumor Microenvironment in Intrahepatic

524 Cholangiocarcinoma. **72**, 965-981 (2020).

525

526 19. Wright G, *et al.* A Probabilistic Classification Tool for Genetic Subtypes of Diffuse

527 Large B Cell Lymphoma with Therapeutic Implications. **37**, 551-568.e514 (2020).

528

529 20. Guruprasad P, Lee Y, Kim K, Ruella MJTJoem. The current landscape of single-cell

- 530 transcriptomics for cancer immunotherapy. **218**, (2021).
- 531
- 532 21. Lin W, *et al.* Single-cell transcriptome analysis of tumor and stromal compartments of
- 533 pancreatic ductal adenocarcinoma primary tumors and metastatic lesions. *Genome*
- 534 *Med* **12**, 80 (2020).
- 535
- 536 22. Stoeckius M, *et al.* Simultaneous epitope and transcriptome measurement in single
- 537 cells. **14**, 865-868 (2017).
- 538
- 539 23. Butler A, Hoffman P, Smibert P, Papalexi E, Satija RJNb. Integrating single-cell
- 540 transcriptomic data across different conditions, technologies, and species. **36**,
- 541 411-420 (2018).
- 542
- 543 24. Jerby-Amon L, *et al.* A Cancer Cell Program Promotes T Cell Exclusion and
- 544 Resistance to Checkpoint Blockade. **175**, 984-997.e924 (2018).
- 545
- 546 25. Peng J, *et al.* Single-cell RNA-seq highlights intra-tumoral heterogeneity and
- 547 malignant progression in pancreatic ductal adenocarcinoma. **29**, 725-738 (2019).
- 548
- 549 26. Zhang X, *et al.* CellMarker: a manually curated resource of cell markers in human and
- 550 mouse. **47**, D721-D728 (2019).
- 551

- 552 27. Zilionis R, *et al.* Single-Cell Transcriptomics of Human and Mouse Lung Cancers
553 Reveals Conserved Myeloid Populations across Individuals and Species. **50**,
554 1317-1334.e1310 (2019).
555
- 556 28. Luoma A, *et al.* Molecular Pathways of Colon Inflammation Induced by Cancer
557 Immunotherapy. **182**, 655-671.e622 (2020).
558
- 559 29. Habib N, *et al.* Disease-associated astrocytes in Alzheimer's disease and aging. *Nat*
560 *Neurosci***23**, 701-706 (2020).
561
- 562 30. Steen CB, Liu CL, Alizadeh AA, Newman AM. Profiling Cell Type Abundance and
563 Expression in Bulk Tissues with CIBERSORTx. *Methods Mol Biol***2117**, 135-157
564 (2020).
565
- 566 31. Hänzelmann S, Castelo R, Guinney JJBb. GSVA: gene set variation analysis for
567 microarray and RNA-seq data. **14**, 7 (2013).
568
- 569 32. Aibar S, *et al.* SCENIC: single-cell regulatory network inference and clustering. **14**,
570 1083-1086 (2017).
571
- 572 33. Efremova M, Vento-Tormo M, Teichmann S, Vento-Tormo RJNp. CellPhoneDB:
573 inferring cell-cell communication from combined expression of multi-subunit

574 ligand-receptor complexes. **15**, 1484-1506 (2020).

575

576 34. Trapnell C, *et al.* The dynamics and regulators of cell fate decisions are revealed by
577 pseudotemporal ordering of single cells. *Nat Biotechnol* **32**, 381-386 (2014).

578

579 35. Gao R, *et al.* Delineating copy number and clonal substructure in human tumors from
580 single-cell transcriptomes. *Nat Biotechnol*, (2021).

581

582 36. Wolford C, *et al.* Transcription factor ATF3 links host adaptive response to breast
583 cancer metastasis. **123**, 2893-2906 (2013).

584

585 37. Pere H, *et al.* A CCR4 antagonist combined with vaccines induces antigen-specific
586 CD8+ T cells and tumor immunity against self antigens. **118**, 4853-4862 (2011).

587

588 38. Berlato C, *et al.* A CCR4 antagonist reverses the tumor-promoting microenvironment
589 of renal cancer. **127**, 801-813 (2017).

590

591 39. Vinci M, *et al.* Functional diversity and cooperativity between subclonal populations of
592 pediatric glioblastoma and diffuse intrinsic pontine glioma cells. *Nat Med* **24**,
593 1204-1215 (2018).

594

595 40. Rubio-Perez C, *et al.* Immune cell profiling of the cerebrospinal fluid enables the

596 characterization of the brain metastasis microenvironment. **12**, 1503 (2021).

597

598 41. Chen YP, *et al.* Single-cell transcriptomics reveals regulators underlying immune cell
599 diversity and immune subtypes associated with prognosis in nasopharyngeal
600 carcinoma. *Cell Res* **30**, 1024-1042 (2020).

601

602 42. Cook PJ, *et al.* Cox-2-derived PGE2 induces Id1-dependent radiation resistance and
603 self-renewal in experimental glioblastoma. *Neuro Oncol* **18**, 1379-1389 (2016).

604

605 43. Jin S, Borkhuu O, Bao W, Yang YT. Signaling Pathways in Thyroid Cancer and Their
606 Therapeutic Implications. *J Clin Med Res* **8**, 284-296 (2016).

607

608 44. Yu J, Baron V, Mercola D, Mustelin T, Adamson ED. A network of p73, p53 and Egr1
609 is required for efficient apoptosis in tumor cells. *Cell Death Differ* **14**, 436-446 (2007).

610

611 45. Jung SN, *et al.* EGR1/GADD45alpha Activation by ROS of Non-Thermal Plasma
612 Mediates Cell Death in Thyroid Carcinoma. *Cancers (Basel)* **13**, (2021).

613

614 46. Crawford NT, McIntyre AJ, McCormick A, D'Costa ZC, Buckley NE, Mullan PB. TBX2
615 interacts with heterochromatin protein 1 to recruit a novel repression complex to
616 EGR1-targeted promoters to drive the proliferation of breast cancer cells. *Oncogene*
617 **38**, 5971-5986 (2019).

618

619 47. Ryu JW, *et al.* Paradoxical induction of growth arrest and apoptosis by EGF via the
620 up-regulation of PTEN by activating Redox factor-1/Egr-1 in human lung cancer cells.
621 *Oncotarget* **8**, 4181-4195 (2017).

622

623 48. Peng WX, *et al.* Egr-1 regulates irradiation-induced autophagy through Atg4B to
624 promote radioresistance in hepatocellular carcinoma cells. *Oncogenesis* **6**, e292
625 (2017).

626

627 49. Gonzalez-Navajas JM, *et al.* The Impact of Tregs on the Anticancer Immunity and the
628 Efficacy of Immune Checkpoint Inhibitor Therapies. *Front Immunol* **12**, 625783 (2021).

629

630 50. Antonelli A, Ferrari SM, Fallahi P. Current and future immunotherapies for thyroid
631 cancer. *Expert Rev Anticancer Ther* **18**, 149-159 (2018).

632

633 51. Lv M, *et al.* Manganese is critical for antitumor immune responses via cGAS-STING
634 and improves the efficacy of clinical immunotherapy. *Cell Res* **30**, 966-979 (2020).

635

636 52. Marigo I, *et al.* T Cell Cancer Therapy Requires CD40-CD40L Activation of Tumor
637 Necrosis Factor and Inducible Nitric-Oxide-Synthase-Producing Dendritic Cells.
638 *Cancer Cell* **30**, 377-390 (2016).

639

- 640 53. Cortez MA, *et al.* Bone morphogenetic protein 7 promotes resistance to
641 immunotherapy. *Nat Commun* **11**, 4840 (2020).
642
- 643 54. Huang Z, *et al.* IL-27 promotes the expansion of self-renewing CD8(+) T cells in
644 persistent viral infection. *J Exp Med* **216**, 1791-1808 (2019).
645
- 646 55. Lei Q, Wang D, Sun K, Wang L, Zhang Y. Resistance Mechanisms of Anti-PD1/PDL1
647 Therapy in Solid Tumors. *Front Cell Dev Biol* **8**, 672 (2020).
648
- 649 56. Severson JJ, *et al.* PD-1+Tim-3+ CD8+ T Lymphocytes Display Varied Degrees of
650 Functional Exhaustion in Patients with Regionally Metastatic Differentiated Thyroid
651 Cancer. *Cancer Immunol Res* **3**, 620-630 (2015).
652
- 653 57. Tirosh I, *et al.* Dissecting the multicellular ecosystem of metastatic melanoma by
654 single-cell RNA-seq. **352**, 189-196 (2016).
655
- 656 58. Liu Y, Cao X. Characteristics and Significance of the Pre-metastatic Niche. *Cancer*
657 *Cell* **30**, 668-681 (2016).
658
659

660 **Acknowledgments**

661 This work was supported by Shanghai Municipal Commission of Health and Family
662 Planning Commission (2019SY062).

663 **Authors' contributions**

664 BH J, ZS W, ZQ Y, and Y R conceived and designed the study. WL J, CG T, and ZS
665 W contributed to carry out the experiments. BH J, CG H, and C Y contributed to data
666 analysis. ZS W, BH J, and ZQ Y wrote the manuscript. YR, WL J, and ZQ Y revised
667 the paper. All authors read and approved the final manuscript.

668 **Competing Interests**

669 The authors have declared that no competing interest exists.

670

671 **Figure legends**

672 **Fig.1 Overall design and single cell atlas in papillary thyroid carcinoma. a**

673 Workflow diagram showing the processing of samples. **b** UMAP plots of total cells,
674 colored by the sample origin (tumor, metastatic LN, and paracancerous tissues). **c**
675 Expression of cell marker genes. **d** Changes in frequency of multiple cell types and
676 clusters in tumors and metastatic LNs. Asterisks on the left of the vertical line denote
677 statistically significant differences between tumors and paracancerous tissues while
678 asterisks on the right are used to show statistically significant differences between
679 metastatic LNs and tumors. * $p < 0.05$, ** $p < 0.01$, *** $p < 0.001$, two-tailed t-tests. **e**
680 Interaction network constructed by CellPhoneDB. Size of circles and color of arrows
681 represent interaction counts, and brighter color and larger size mean more interaction
682 with other cell types.

683 **Fig.2 Identification of malignant cells in epithelial cells. a**

684 epithelial cells delineated by clustering single-cell copy number profiles inferred from
685 scRNA-seq data by CopyKAT. **b** UMAP plots of total epithelial cells, colored by the
686 sample origin (left and middle). Cell counts of malignant and non-malignant cells,
687 colored by the sample origin (right). **c** Differentiation trajectory of epithelial cells,
688 with each color coded for pseudotime (right) and clusters (left). **d** Heatmap of the area
689 under the curve (AUC) scores of transcription factor (TF) motifs estimated by
690 SCENIC. Shown are differentially activated motifs in malignant and non-malignant
691 cells, respectively. **e** High level of CREM and ETS1 predicted good prognosis in the
692 TCGA THCA cohort. Log-rank p value < 0.05 was considered as statistically
693 significant. **f** BHLHE40 was highly expressed in LN samples ($p < 0.001$). **g** GO
694 enrichment analysis of up-regulated genes in malignant lymphatic metastasis cells.

695 **Fig.3 Heterogeneity of T cell populations. a**

696 UMAP plot of T cells color-coded by
697 their associated cell types. **b** Dotplot of cell markers; sizes of dots represent
698 abundance while color represents expression level. **c** Potential new cell markers. **d**
699 The protein level of EGR1 was decreased in tumor tissues compared with normal
700 tissues. **e** High level of EGR1 predicted good prognosis in the TCGA THCA cohort.
701 **f** Changes in frequency of multiple cell types in T cell populations. Asterisks on the
702 left of the vertical line denote statistically significant differences between tumors and
703 paracancerous tissues while asterisks on the right are used to show statistically
704 significant differences between LNs and tumors. * $p < 0.05$, ** $p < 0.01$, *** $p < 0.001$,
two-tailed t-tests. **g** Violin of cell abundance predicted from the TCGA THCA cohort

by CIBERSORTx.

Fig.4 Novel cell type, named Protective EGR1⁺CD4⁺ T cells, and potential therapeutic targets. **a** Differences in 50 hallmark pathway activities scored with GSVA software. Shown are t values calculated by a linear model. **b** Heatmap of the AUC scores of TF motifs estimated by SCENIC. Shown are differentially activated motifs in CD4⁺ Tregs and Protective EGR1⁺CD4⁺ T cells, respectively. **c-d** Heatmap of positive and negative immune checkpoint expression on T cells in LNs (**c**) and tumors (**d**), respectively.

Fig.5 Heterogeneity of Myeloid cell populations. **a** UMAP plot of Myeloid cells color-coded by their associated cell types. **b** Dotplot of cell markers; sizes of dots represent abundance while color represents expression level. **c** Changes in frequency of multiple cell types and clusters in Myeloid cell populations. Asterisks on the left of the vertical line denote statistically significant differences between tumors and paracancerous tissues while asterisks on the right are used to show statistically significant differences between LNs and tumors. *p < 0.05, **p < 0.01, ***p < 0.001, two-tailed t-tests. **d** Violin of Macrophage abundance predicted from the TCGA THCA cohort by CIBERSORTx. **e** Kaplan-Meier curves of DFS based on the percentage of dendritic cells in the TCGA database.

Fig.6 M2 macrophages were strongly enriched in the tumor tissues. **a-b** Heatmap shows the differences in pathway activities scored by GSVA between different sample origins. Shown are t values calculated by a linear model. **c** Heatmap of the AUC scores of TF motifs estimated by SCENIC. Shown are differentially activated motifs in subtypes of Myeloid cells, respectively. **d** Violin plot shows the expression level of related genes in Macrophage subclusters (left) and cytokines in dendritic cells (right).

Supplementary information

Supplementary Fig. 1 Identification of major cell types in PTC. UMAP plots for expression of the marker genes from **Fig 1c** and of additional marker genes for major cell types. For B cells: CD19, MS4A1(CD20), CD38, CD79A, and CD79B; for CD4⁺ T cells: CD4 and CD3D; for CD8⁺T cells: CD8A and CD3D; for Endothelial cells: CD34 and CD31(PECAM); for Epithelial cells: EPCAM and KRT18; for Fibroblasts: COL1A1; for Myeloid cells: CD14, CD86, ITGAX, CD80, CD83, and ITGAM; for Naive T cells: CCR7 and CD3D; for NKT cells: NKG7 and CD3D; for Plasma cells:

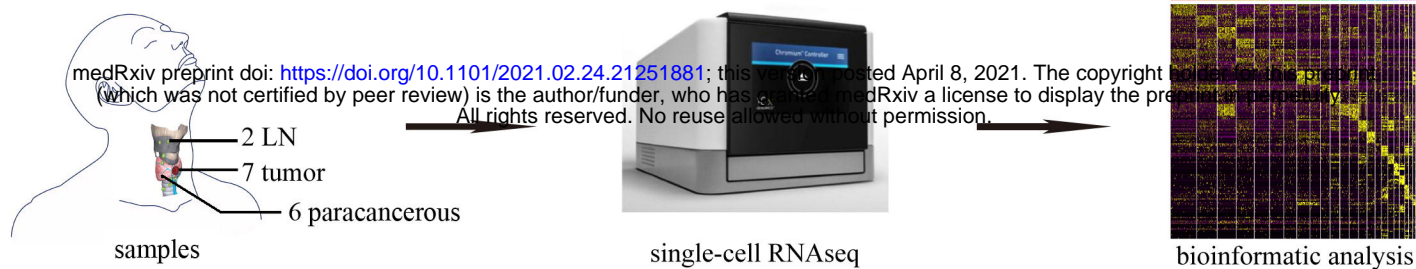
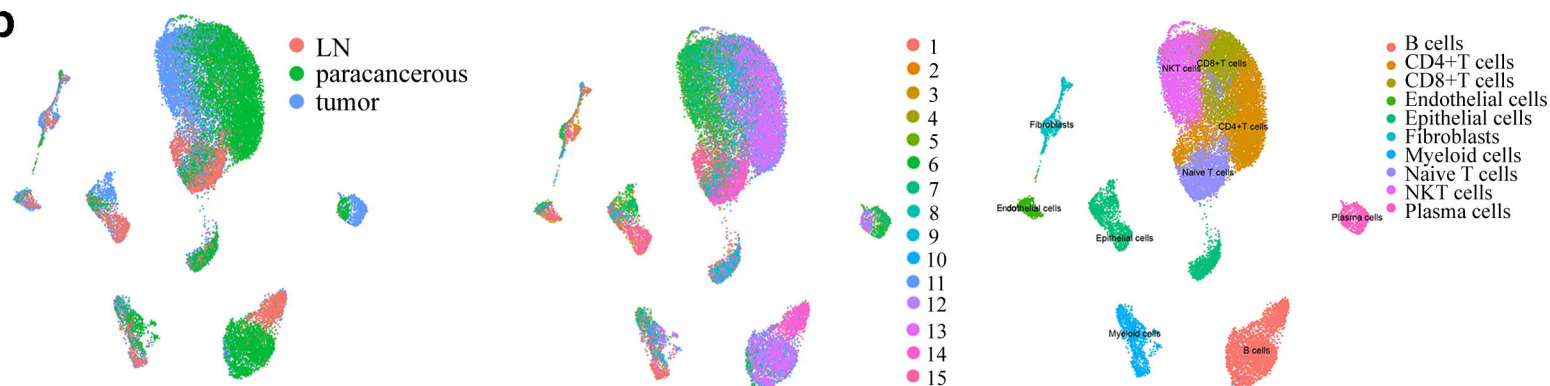
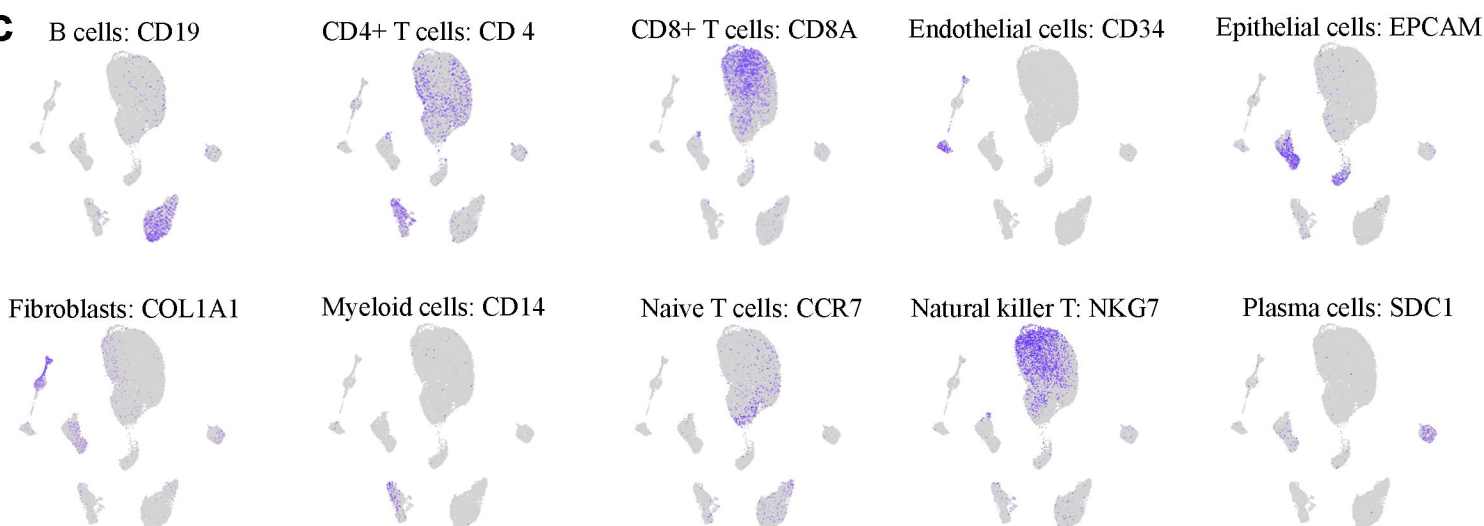
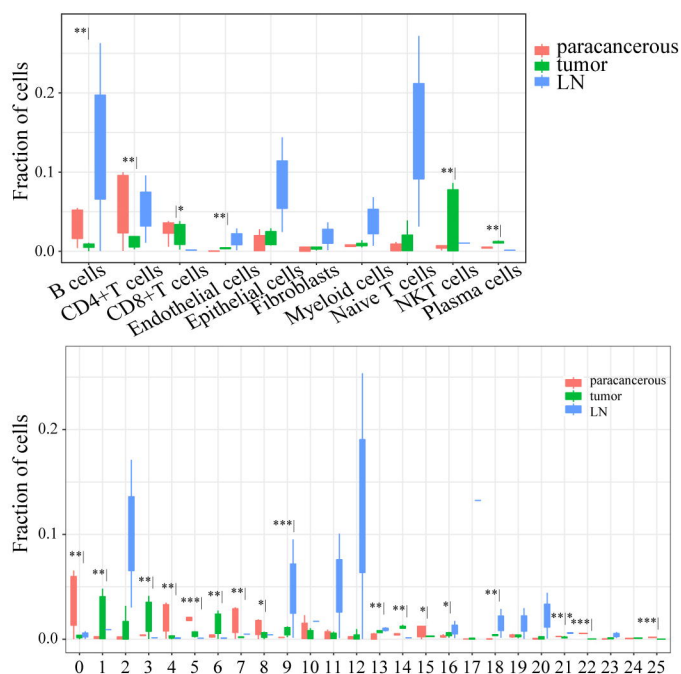
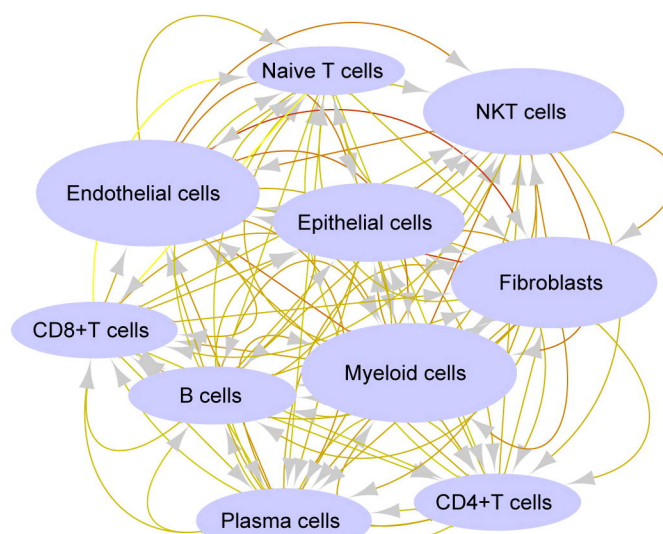
737 CD79A and SDC1.

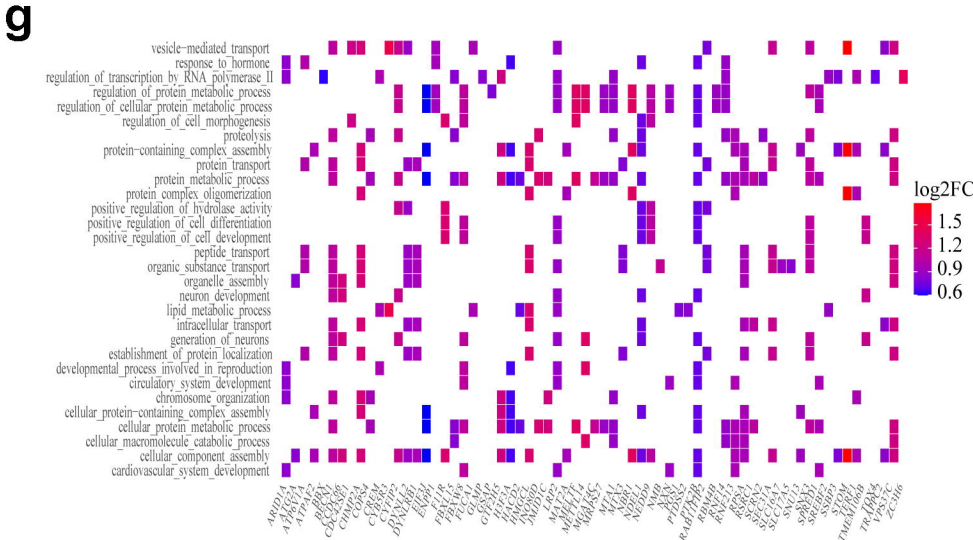
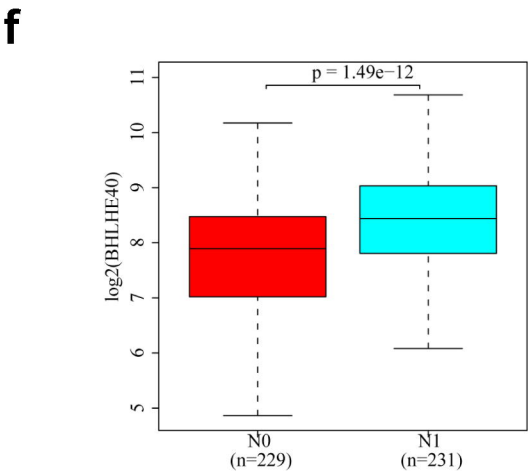
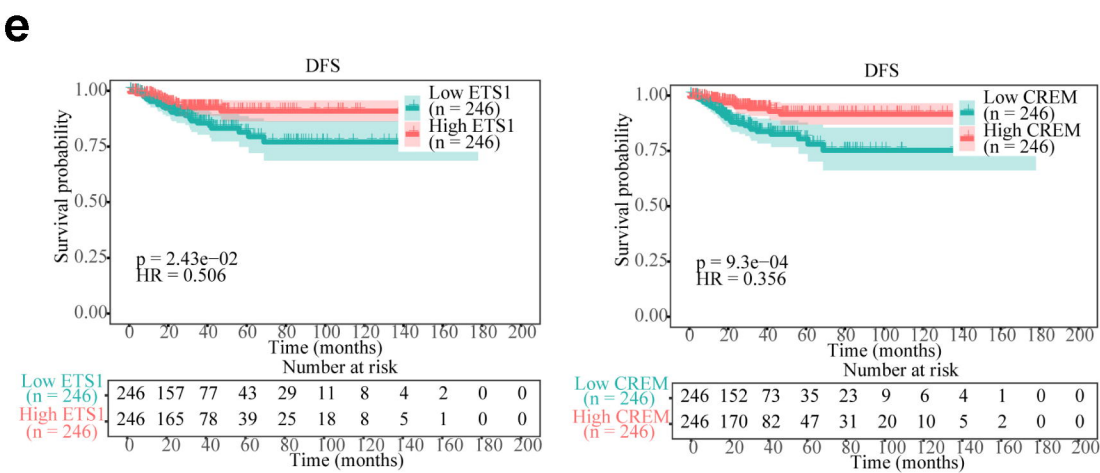
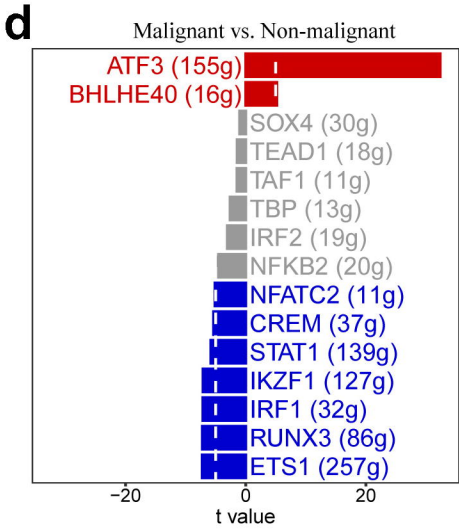
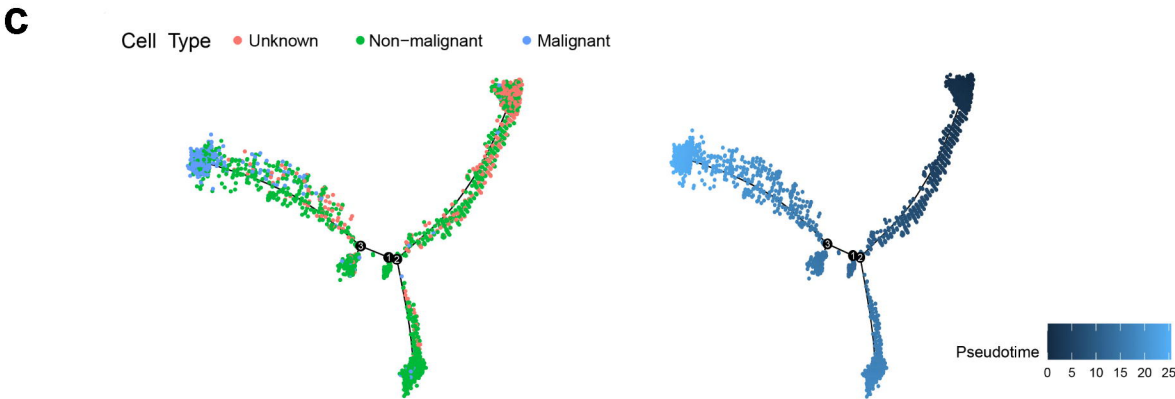
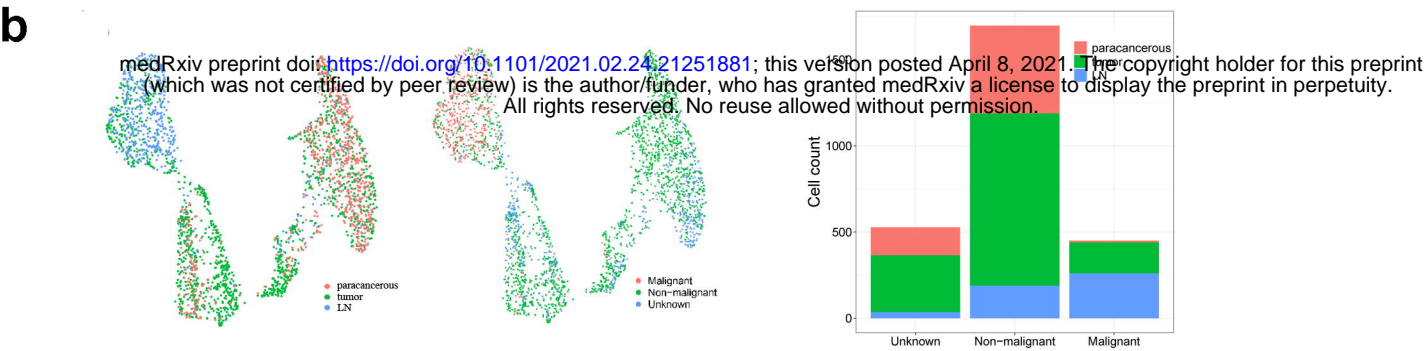
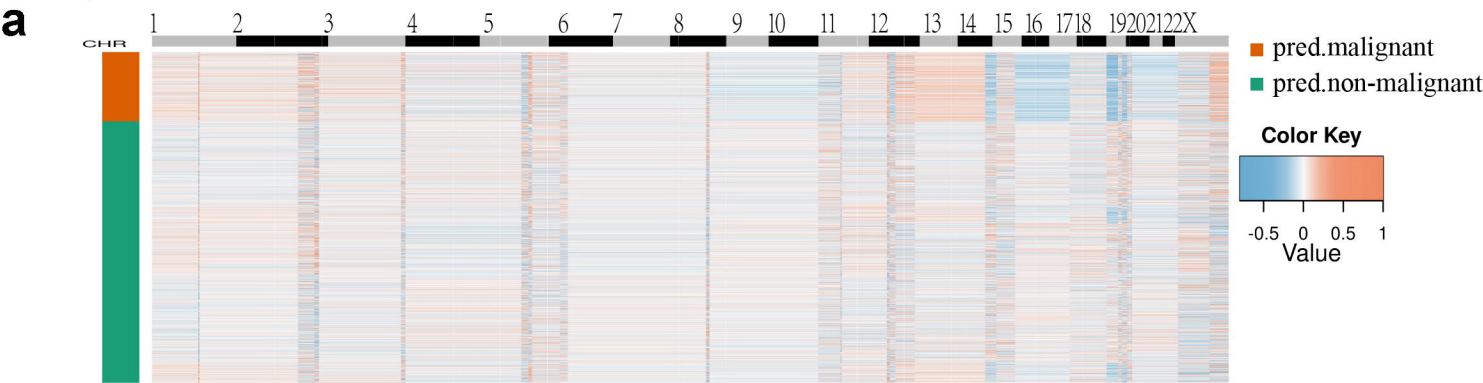
738 **Supplementary Fig. 2 Overview of the 28,205 single cells from tumors,**
 739 **paracancerous tissues, and metastatic LNs. a** The fraction of multiple cell types
 740 originating from 7 tumor tissues, 6 paracancerous tissues, and 2 metastatic LNs. **b** The
 741 fraction of multiple cell types originating from 15 samples. **c** The number of multiple
 742 cell types. **d** Box plots of the number of transcripts.

743 **Supplementary Fig. 3 Potential new cell markers in T cells.**

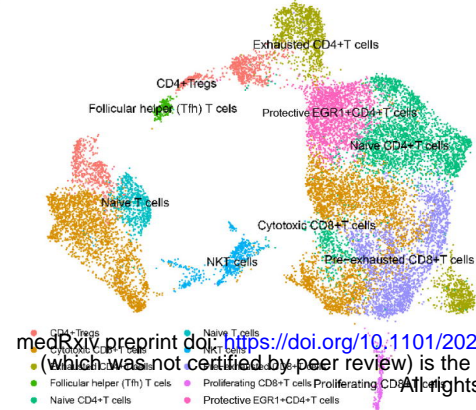
744 **Supplementary Fig. 4 DEGs related to CD4⁺Tregs and transitional EGR1⁺CD4⁺T**
 745 **cells. a** The expression of the marker genes in the TCGA THCA cohort. **b** Differences
 746 in 50 hallmark pathway activities scored with GSEA software. Shown are t values
 747 calculated by a linear model. **c** DEGs related to Protective EGR1⁺CD4⁺ T cells in
 748 tumors and LNs, respectively. **d** DEGs related to CD4⁺Tregs in tumors and LNs,
 749 respectively. Upregulated genes and downregulated genes were colored in red and
 750 blue, respectively. $FC \geq 2$.

751 **Supplementary Fig. 5 External verification based on the TCGA data. a** High level
 752 of Macrophage abundance predicted poor prognosis in the TCGA THCA cohort, and
 753 neutrophil was the opposite. **b** Kaplan-Meier survival curve for IFITM2.

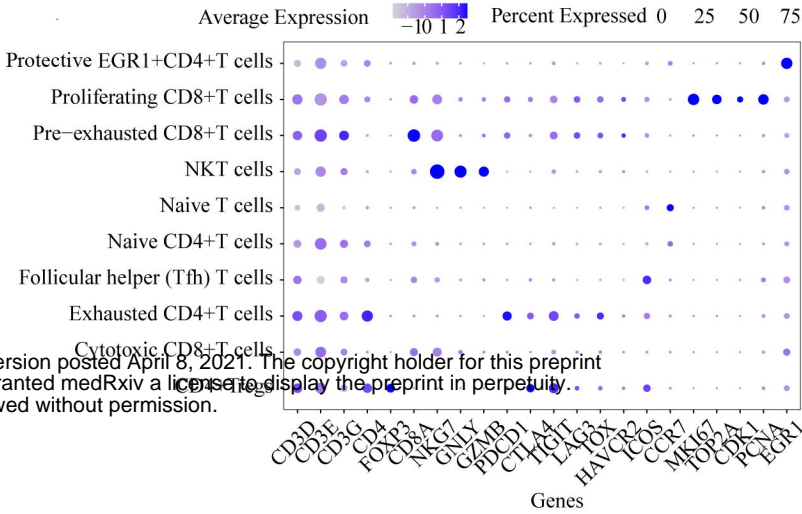
a**b****c****d****e**



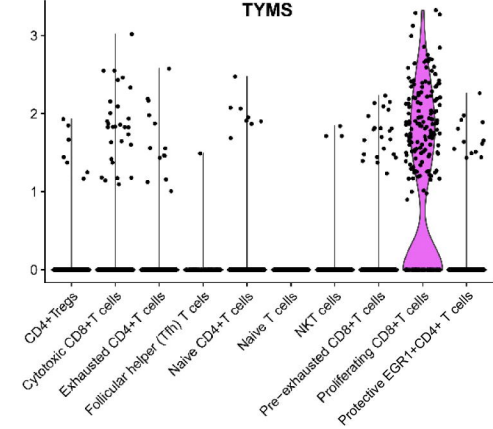
a



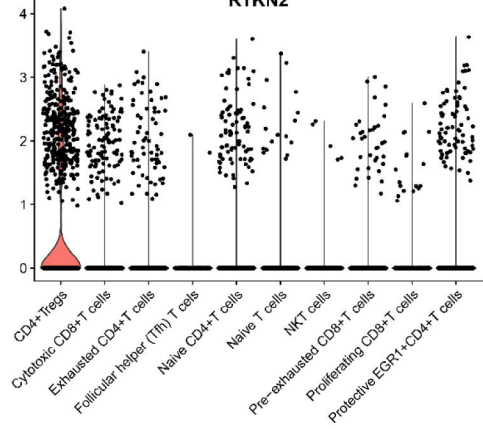
b



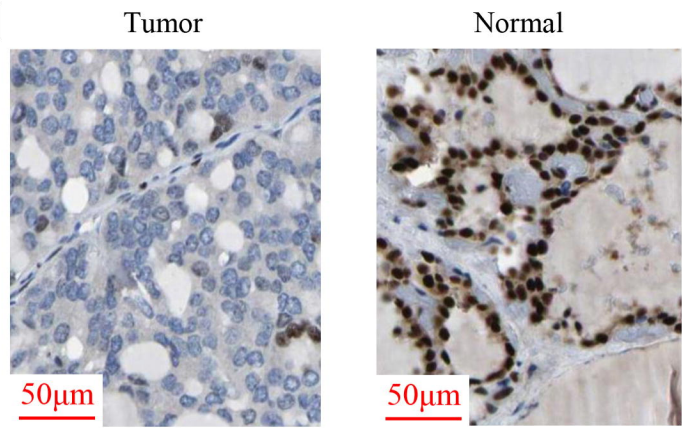
c



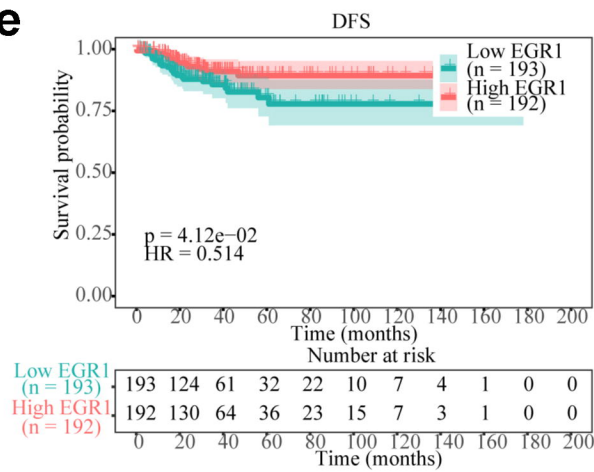
RTKN2



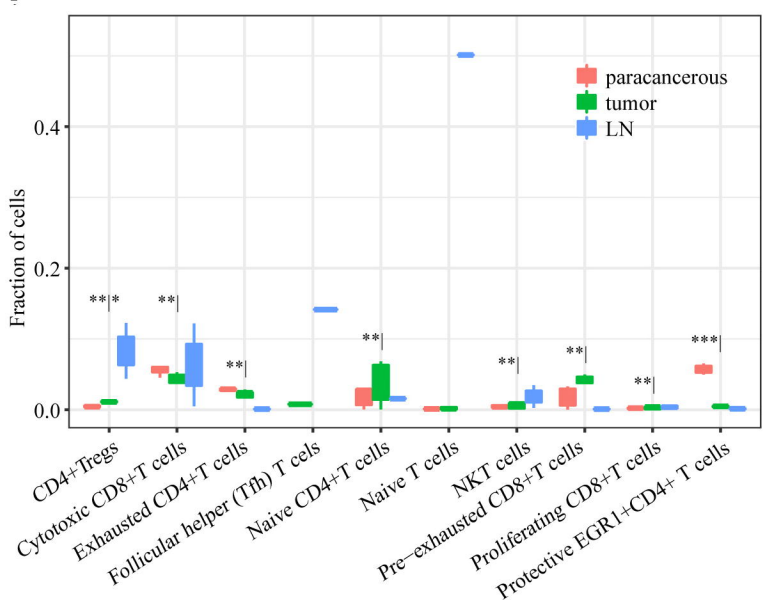
d



e



f



g

